

A kinetic study of the gas-phase C(³P) + CH₃CN reaction at low temperature. Rate constants, H-atom product yields and astrochemical implications

Kevin M. Hickson,^{1,*} Jean-Christophe Loison¹ and Valentine Wakelam²

¹Institut des Sciences Moléculaires ISM, CNRS UMR 5255, Univ. Bordeaux, 351 Cours de la Libération, F-33400, Talence, France

²Laboratoire d'astrophysique de Bordeaux, CNRS, Univ. Bordeaux, B18N, allée Geoffroy Saint-Hilaire, F-33615 Pessac, France

Abstract

Rate constants have been measured for the C(³P) + CH₃CN reaction between 50 K and 296 K using a continuous-flow supersonic reactor. C(³P) atoms were created by the *in-situ* pulsed laser photolysis of CBr₄ at 266 nm, while the kinetics of C(³P) atom loss were followed by direct vacuum ultra-violet laser induced fluorescence at 115.8 nm. Secondary measurements of product H(²S) atom formation were also made, allowing absolute H-atom yields to be obtained by comparison with those obtained for the C(³P) + C₂H₄ reference reaction. In parallel, quantum chemical calculations were performed to obtain the various complexes, adducts and transition states relevant to the title reaction over the ³A'' potential energy surface, allowing us to better understand the preferred reaction pathways. The reaction is seen to be very fast, with measured rate constants in the range $(3-4) \times 10^{-10} \text{ cm}^3 \text{ s}^{-1}$ with little or no observed temperature dependence. As the C + CH₃CN reaction is not considered in current astrochemical networks, we test its influence on interstellar methyl cyanide abundances using a gas-grain dense interstellar cloud model. Its inclusion leads to predicted CH₃CN abundances that are significantly lower than the observed ones.

Introduction

Almost 40 % of all molecules detected in interstellar space contain the element nitrogen, while nitrogen-bearing organic compounds are essential for life on Earth due to the role of nitrogen in proteins, DNA and other vital materials.

Amongst the multitude of nitrogen containing species present in the Earth's atmosphere, Methyl cyanide (also known as acetonitrile, CH_3CN) and hydrogen cyanide (HCN) are important trace gases of anthropogenic origin. Indeed, as a strongly polar liquid at room temperature, CH_3CN is a common solvent in research and industrial applications. Due to its relatively low reactivity with important radicals such as OH^1 and Cl^2 , CH_3CN is thought to have a long tropospheric lifetime of 3 years³ allowing this species to be transported to the stratosphere.⁴ CH_3CN , which was first detected in the interstellar medium in 1971 by Solomon et al.⁵ towards Sgr A and B has also been observed in numerous other astrophysical objects such as dense molecular clouds,⁶ in protoplanetary disks,⁷ in cometary coma⁸ and in planetary atmospheres such as Titan.⁹ Isotopologues such as the singly deuterated form $\text{CH}_2\text{DCN}^{10}$ have also been observed towards the hot core of IRc2 in OMC1, $^{13}\text{CH}_3\text{CN}$, $\text{CH}_3^{13}\text{CN}$ and CH_3^{15}N in the protostar IRAS-16293¹¹ and CH_3^{15}N in Titan's atmosphere.¹² A survey of molecular observations in dark cloud TMC-1 determined an abundance of CH_3CN of 2×10^{-10} relative to total hydrogen ($n\text{H} + 2n\text{H}_2$),¹³ similar to other complex organic molecules such as CH_3OH and CH_3CHO . Given its widespread presence in interstellar environments, this species is expected to play an active role in the chemistry. As H, C, N and O atoms are all considered to be among the most abundant species in the interstellar medium, the reactions of CH_3CN with any of these atomic radicals could represent significant formation and loss processes in these regions. Previous work has shown that the reactions of CH_3CN with $\text{H}(^2\text{S})^{14}$ and $\text{O}(^3\text{P})^{15}$ are slow at room temperature and above, being characterized by an activation barrier, while the

reactions of $N(^4S)$ with closed shell molecules are typically very slow.¹⁶ In contrast, there appears to be no earlier work on the $C(^3P) + CH_3CN$ reaction in the scientific literature, so its influence on interstellar chemistry is currently unknown. In related work however, an ab-initio study of the HCCN system by Loison and Hickson¹⁷ indicated that at the various theoretical levels employed, attack of the CN triple bond by atomic carbon in the $C + HCN$ reaction was barrierless although all possible exit channels of this reaction are endothermic (other than the isotope exchange channel) unlike the $C + HNC$ reaction which was calculated to be a barrierless process leading to the products $C + HCN$ by isomerization.

To evaluate the importance of the reaction between C-atoms and CH_3CN in interstellar environments, we performed a joint experimental and theoretical study of this process. Experimentally, a supersonic flow reactor coupled with pulsed laser photolysis production and direct laser induced fluorescence detection was employed to follow the kinetics of atomic carbon loss in the presence of CH_3CN down to low temperature. Additionally, the kinetics of H-atom formation was also followed by laser induced fluorescence, allowing absolute H-atom product yields to be determined at two different temperatures through comparison with a reference reaction. On the theoretical side, electronic structure calculations were performed to obtain the energies of the relevant intermediates, transition states and complexes over the $^3A''$ potential energy surface of C_3H_3N connecting reagents to products. The effects of the $C + CH_3CN$ reaction on interstellar chemistry were tested using an astrochemical model containing both gas-phase and grain surface processes. Sections 2 and 3 outline the experimental and theoretical methodologies respectively. Section 4 presents the experimental and theoretical results and discusses these results in the context of the electronic structure calculations. The astrochemical implications of the current work are presented in section 5, while our conclusions are described in section 6.

2 Experimental Methods

The continuous supersonic flow method, also known as the CRESU technique (cinétique de réaction en écoulement supersonique uniforme or reaction kinetics in a uniform supersonic flow) was used to study the kinetics of the $C(^3P) + CH_3CN$ reaction. The present apparatus has been described in detail in previous work,^{18,19} while the various modifications that have enabled us to follow the reaction kinetics of several different atomic radicals are described in later work.²⁰⁻³⁹ The CRESU technique relies on the use of Laval type nozzles employing specified carrier gases (Ar or N₂) to generate flows with uniform densities, velocities and constant low temperatures as a function of distance. During this study, three different nozzles allowed us to perform measurements at 50 K, 75 K, 127 K and 177 K (one nozzle was used with both carrier gases). The nozzle flow characteristics are summarized in Table 2 of Hickson et al.²¹ (the 106 K nozzle was not used here). Additionally, by using the reactor as a conventional slow-flow apparatus, it was also possible to perform measurements at room temperature (296 K).

In previous experiments employing liquid coreagents at room temperature,^{20,22} a spectroscopic method involving absorption of the 185 nm line of a mercury lamp was employed to determine the gas-phase coreagent concentration. In the present case, the CH₃CN absorption cross-section is too weak above 160 nm, making it impossible to derive its gas-phase concentration spectroscopically. Instead, a small flow of carrier gas was bubbled through coreagent CH₃CN held at room temperature and into a cold finger held at 290 K and a known pressure. In this way, we ensured that the CH₃CN saturated vapour pressure was attained, allowing its gas-phase concentration to be determined accurately by the expression

$$F_{\text{CH}_3\text{CN}} = F_{\text{CG}} \times \frac{P_{\text{CH}_3\text{CN}}}{P_{\text{TOT}} - P_{\text{CH}_3\text{CN}}}$$

where $F_{\text{CH}_3\text{CN}}$ is the calculated CH_3CN flow, F_{CG} is the carrier gas flow rate, $P_{\text{CH}_3\text{CN}}$ is the saturated vapour pressure of CH_3CN (at 290 K)⁴⁰ and P_{TOT} is the total bubbler pressure. To prevent condensation downstream of the bubbler, the CH_3CN laden carrier gas was passed through a heating hose held at 353 K before entering the reactor. Upon entering the nozzle reservoir, the CH_3CN was further diluted by the main carrier gas flow, so we assume no further condensation occurred in this region.

Tetrabromomethane (CBr_4) was used as the source of ground state carbon atoms during this work. A small fraction of the carrier gas flow was diverted into a flask at a known fixed temperature and pressure containing solid CBr_4 , with the output connected to the Laval nozzle reservoir. CBr_4 was estimated to be present in the supersonic flow at concentrations less than $2.6 \times 10^{13} \text{ cm}^{-3}$ based on its saturated vapour pressure. The output of an unfocused frequency quadrupled pulsed Nd:YAG laser at 266 nm (21 mJ/pulse) was aligned along the axis of the supersonic flow, producing $\text{C}(^3\text{P})$ atoms by the photodissociation of CBr_4 molecules in a sequential multiphoton process. $\text{C}(^1\text{D})$ atoms were also produced by CBr_4 photolysis. Previous work performed under similar conditions²⁰ indicate that the ratio $\text{C}(^1\text{D})/\text{C}(^3\text{P})$ should be around 0.1-0.15.

Two different types of experiments were performed during this work. Firstly, by following the decay of $\text{C}(^3\text{P})$ atoms in the presence of coreagent CH_3CN , temperature dependent rate constants could be determined. Secondly, by following the formation of $\text{H}(^2\text{S})$, it was possible to determine temperature dependent branching fractions for those product channels leading to H-atoms. In earlier experiments,²⁰⁻²² $\text{C}(^3\text{P})$ atoms were detected by resonant laser induced fluorescence in the vacuum ultraviolet (VUV LIF) using the $2s^2 2p^2 \ ^3\text{P}_2 \rightarrow 2s^2 2p3d \ ^3\text{D}_3^\circ$ transition at 127.755 nm. Here, the $2s^2 2p^2 \ ^3\text{P}_2 \rightarrow 2s^2 2p5d \ ^3\text{D}_3^\circ$ transition at 115.803 nm was

employed instead, which allowed us to use the same set of beam-steering optics as those used for all our kinetic studies of atomic radical ($\text{H}(^2\text{S})$, $\text{N}(^2\text{D})$ and $\text{O}(^1\text{D})$) reactions. Tuneable narrowband radiation at 115.8 nm was generated from a 10 Hz Nd:YAG pumped dye laser operating around 695 nm. The fundamental dye laser beam was frequency doubled in a beta barium borate (BBO) crystal, with the residual dye laser radiation being separated from the 347 nm UV beam by two dichroic mirrors with a coating optimized for reflection at 355 nm. The 347 nm beam was then directed and focused into a cell attached at the level of the observation axis containing 50 Torr of xenon with 160 Torr of argon added for phase matching purposes. For the product yield measurements, $\text{H}(^2\text{S})$ atoms were followed by pulsed VUV LIF at 121.567 nm generated by frequency tripling following the procedure described in earlier work.^{20, 22-24, 26-30, 41} using a mixture containing 210 Torr of krypton and 540 Torr of argon. The VUV beams generated by these procedures were collimated by a MgF_2 lens which also served as the cell exit window. The cell itself was attached to the reactor by a 75 cm long sidearm containing diaphragms, thereby blocking a large fraction of the divergent UV beam before it could enter the reactor. As significant attenuation of the VUV beam by residual gases occurred in this region, it was constantly flushed with nitrogen or argon. The VUV beam was adjusted to intersect the cold supersonic flow at right angles on entering the reactor, while the detector, a solar blind photomultiplier tube (PMT), was positioned at right angles to both the flow and the VUV beam to minimize the detection of scattered VUV and UV radiation. An LiF window isolated the PMT from the reagents within the chamber, while an LiF lens positioned behind this window was used to focus the VUV emission from $\text{C}(^3\text{P})$ or $\text{H}(^2\text{S})$ atoms onto the PMT photocathode. This region was constantly evacuated to prevent attenuation of the VUV emission by atmospheric oxygen. Moreover, several diaphragms were placed throughout the detection system to minimize the detection of scattered light. The VUV LIF

signals received by the PMT were recorded as a function of the time between the photolysis and probe lasers which were controlled with a precision on the picosecond timescale by a digital delay generator. For each individual time point, 30 VUV LIF signals were averaged, with at least 70 time points recorded for each individual temporal profile. The maximum exploitable time for these decays depended on the individual nozzle used. Consequently, the Laval nozzles were positioned at the maximum distance from the observation axis where optimal flow conditions were still considered to be valid. These distances were derived in earlier characterization experiments where the impact pressure measured by a Pitot tube was recorded as a function of distance from the Laval nozzle. The carrier gas flows Ar (Messer 99.999 %) and N₂ (Air Liquide 99.999 %) and the reactive gas C₂H₄ (Messer 99.95 %) were regulated by calibrated mass-flow controllers. All gases including the Xe (Linde 99.999 %) and Kr (Linde 99.999 %) used in the tripling cell were flowed directly from gas cylinders without further purification.

3 Theoretical Methods

The reagents C(³P_{0,1,2}) and CH₃CN(¹A') correlate with 3 potential energy surfaces, one ³A' and two ³A'' surfaces in C_s symmetry. Entrance channel calculations were performed at the MRCI+Q/AVDZ level (Davidson corrected multi-reference configuration interaction (MRCI + Q) with complete active space self-consistent field (CASSCF) wave-functions associated to the AVDZ basis set using an active space consisting of 8 electrons distributed in 8 orbitals. The 8 orbitals employed are the 2p_z of nitrogen (rather a hybrid 2s-2p_z orbital of nitrogen, the z axis being the axis of the C-N bond) corresponding to the orbitals of the free doublet of nitrogen of the CN bond, to the π orbitals of the CN triple bond (two bonding π_{x,y} and two antibonding π*_{x,y} orbitals) and finally to the three 2p_x, 2p_y and 2p_z orbitals of the isolated carbon atom. It

is important to include the non-bonding orbital of the nitrogen atom of CN containing the lone electron pair to describe the interaction with the $2p_z$ orbital of the carbon atom colliding with CH_3CN , correlating with the sigma $\text{CH}_3\text{CN-C}$ bond. The π and π^* orbitals of the CN bond interact with the $2p_x$ and $2p_y$ atomic orbitals of carbon correlating with the Π system of the C=N=C group. It has been found that only the first $^3A''$ surface was found to be attractive for the approach of atomic carbon to the nitrogen atom of CH_3CN leading to CH_3CNC .

The absence of a barrier for this reaction was obtained at the MRCI level by partially optimizing the geometry at the CASCCF level. The optimized parameters were all distances and angles except the dihedral angles, the parameters being set to maintain a C_s geometry when the carbon atom approaches the nitrogen atom (between 10 and 1.8 angstrom with variable steps between 0.1 and 1 angstrom depending on the distance. At this level of computation, the most favourable approach is for a $\text{CH}_3\text{C-N-C}$ angle close to 180° . The first step of the reaction is therefore the barrierless formation of CH_3CNC . To describe the evolution of this adduct we have calculated the global pathways connecting $\text{C} + \text{CH}_3\text{CN}$ and the various products were calculated using DFT calculations with the M06-2X functional⁴² associated to the AVTZ basis set, leading to the schematic energy diagram shown in Figure 1.

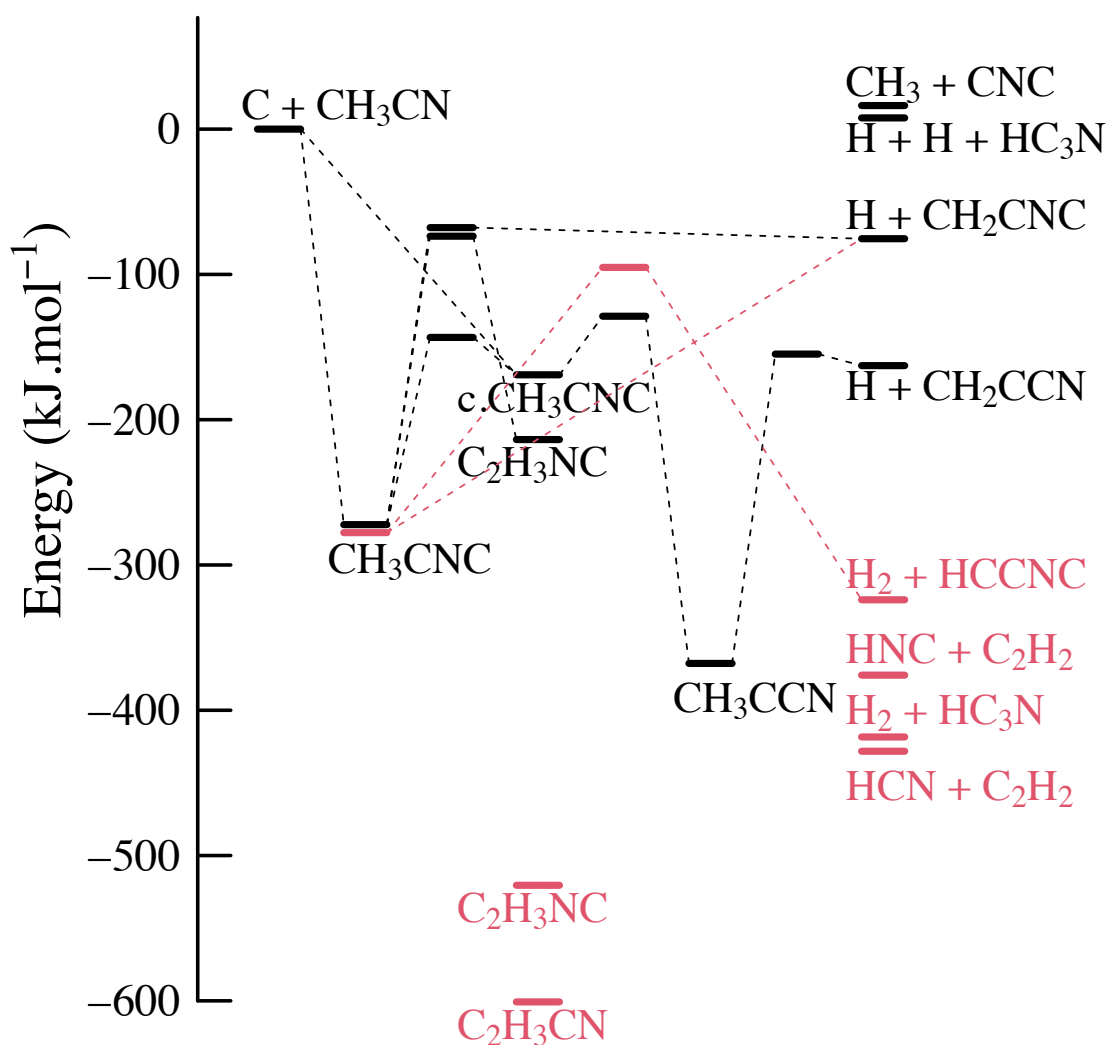


Figure 1 Potential energy diagram for the $C(^3P) + CH_3CN$ reaction over the triplet (black lines) and singlet (red lines) potential energy surfaces of C_3H_3N calculated at the DFT level with the M06-2X functional at the AVTZ level.

In this figure we show the triplet surface which corresponds to the initial pathway of the reaction since the carbon atom is in a triplet state and CH_3CN in a singlet state, but also the singlet surface which correlates to other more stable intermediates and products of the reaction. The singlet surface might play a role in the reaction if the coupling between triplet

and singlet surfaces is important. The initially formed triplet CH_3CNC can evolve through several different pathways. (1) It can form $\text{H} + \text{CH}_2\text{CNC}$ directly over an exit channel transition state (TS) -68 kJ/mol lower in energy than the reagents $\text{C} + \text{CH}_3\text{CN}$. It can isomerize to form (2) $\text{C}_2\text{H}_3\text{NC}$ (over an exit channel transition state (TS) -63 kJ/mol below the reagents $\text{C} + \text{CH}_3\text{CN}$) or (3) into $c\text{-CH}_3\text{CNC}$ (over an exit channel transition state (TS) -144 kJ/mol below the reagents $\text{C} + \text{CH}_3\text{CN}$) and then into CH_3CCN leading ultimately to the products $\text{H} + \text{CH}_2\text{CCN}$. $c\text{-CH}_3\text{CNC}$ can also be produced directly from the $\text{C} + \text{CH}_3\text{CN}$ reagents. As shown in Figure 1, the most stable species on the $\text{C} + \text{CH}_3\text{CN}$ surfaces are $\text{C}_2\text{H}_3\text{NC}$ and $\text{C}_2\text{H}_3\text{CN}$ in their ground singlet states. The minimum energies of the triplet and singlet states of CH_3CNC are found to be very close in this work (within 1 kJ mol⁻¹ at the M06-2X/AVTZ level). Interestingly, the energy of the singlet state of CH_3CNC at the triplet equilibrium geometry, and the energy of the triplet state of CH_3CNC at the singlet equilibrium geometry are also very close (within 5 kJ mol⁻¹ at the M06-2X/AVTZ level) and close to their energy minimum as the equilibrium geometries of both the triplet and singlet states of CH_3CNC are very similar. As the difference in energy between the two surfaces is low and the geometries are similar, intersystem crossing might be promoted, allowing reaction to take place over the singlet surface. Then, as already seen in photodissociation studies of $\text{C}_2\text{H}_3\text{CN}$,⁴³⁻⁴⁵ singlet state products such as $\text{C}_2\text{H}_2 + \text{HCN}$, $\text{C}_2\text{H}_2 + \text{HNC}$, $\text{H}_2 + \text{HC}_3\text{N}$ and also $\text{H}_2 + \text{HCCNC}$ might be accessible. We did not recalculate all the intermediates on the singlet surface but only the $\text{H}_2 + \text{HCCNC}$ formation channel as it was not studied by Homayoon et al.,⁴³ but these products are all accessible from CH_3CNC in its singlet state as shown by the low transition state found at the M06-2X/AVTZ level here.

Although a complete study of the singlet surface is not performed here, selected details are included to show its possible importance. It should be noted that the products $\text{C}_2\text{H}_2 + \text{HCN}$,

$C_2H_2 + HNC$, $H_2 + HC_3N$ and $H_2 + HCCNC$ (where one of the products is formed in a triplet state) are not energetically accessible from the triplet surface as all these channels are endothermic.

4 Experimental Results

4.1 Rate Constants

A low concentration of $C(^3P)$ radicals was employed in the present study with respect to the large excess concentration of CH_3CN . Under these conditions, the CH_3CN concentration was constant so that the $C(^3P)$ VUV LIF signal decayed exponentially to zero as a function of time. This allowed the effective rate law to be simplified from a second-order to a first-order process (the so called pseudo-first-order approximation). Typical decay profiles recorded at 75 K are shown in Figure 2.

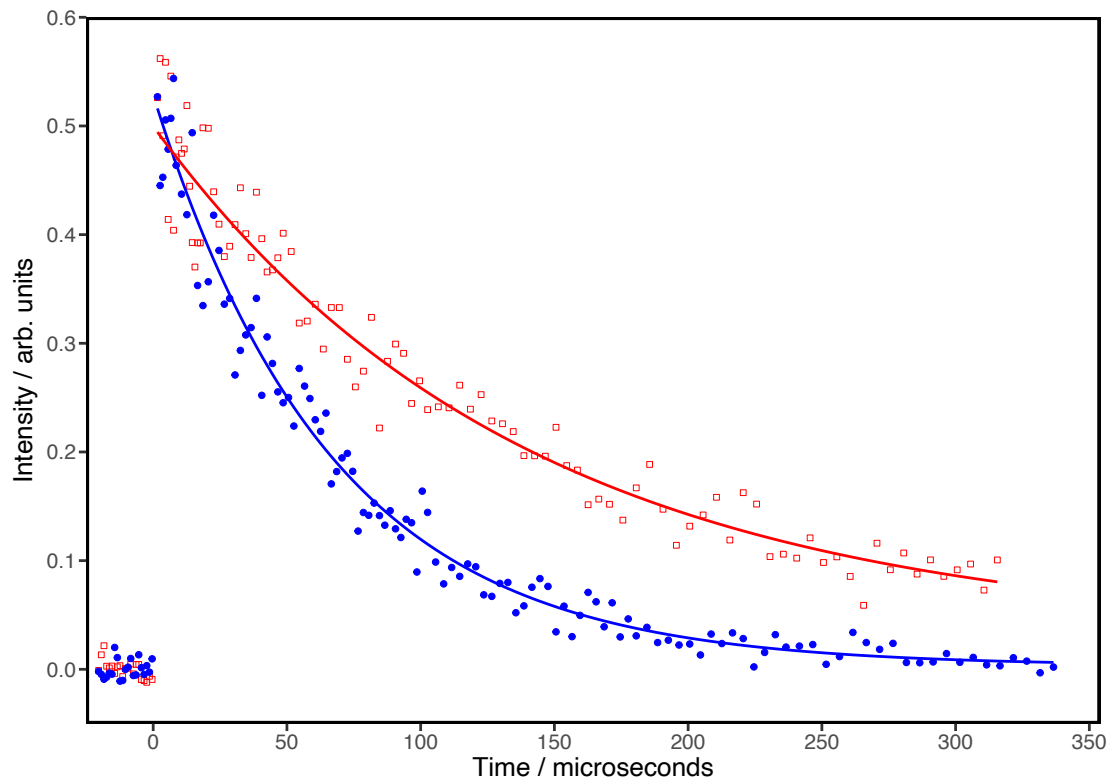


Figure 2 Temporal profiles of the C(³P) VUV LIF intensity measured at 75 K. (Blue solid circles) [CH₃CN] = 1.8 × 10¹³ cm⁻³; (Red open squares) decay recorded in the absence of CH₃CN. Solid lines represent exponential fits to the individual datasets of the form $I = I_0 \exp(-k_{1st}t)$ (see text).

An expression of the form

$$I(t) = I_0 \exp(-k_{1st}t) \quad (1)$$

was used to perform non-linear least-squares fits to the individual decay curves, where $I(t)$ and I_0 are the time-dependent and initial C(³P) fluorescence signals respectively, k_{1st} is the pseudo-first-order rate constant for C-atom loss and t is time. In the present case, k_{1st} represents the sum of several first-order processes. In the absence of CH₃CN (red open squares), C(³P) is lost primarily through diffusion from the detection region with a first-order rate constant k_{diff} (the diameters of the photolysis and probe laser beams are approximately 5-7 mm in the detection region) with possible small secondary contributions from its reaction with the C(³P) precursor CBr₄, $k_{C+CBr_4}[CBr_4]$, and any other impurities present in the carrier gas flow $k_{C+X}[X]$. A clear increase in the reaction rate is observed following the addition of CH₃CN to the flow (blue solid circles) due to the additional contribution of the C(³P) + CH₃CN reaction, $k_{C+CH_3CN}[CH_3CN]$, such that the measured $k_{1st} = k_{C+CH_3CN}[CH_3CN] + k_{C+CBr_4}[CBr_4] + k_{C+X}[X] + k_{diff}$. As [CBr₄], [X] and k_{diff} are constant for any single series of measurements (k_{diff} is constant for any particular set of detection geometries), k_{1st} varies only as a function of [CH₃CN] during the present experiments. For each temperature, at least 10 different CH₃CN concentration values were used. The derived k_{1st} values were plotted as a function of [CH₃CN] as shown in Figure 3 for data recorded at 75 K and 296 K.

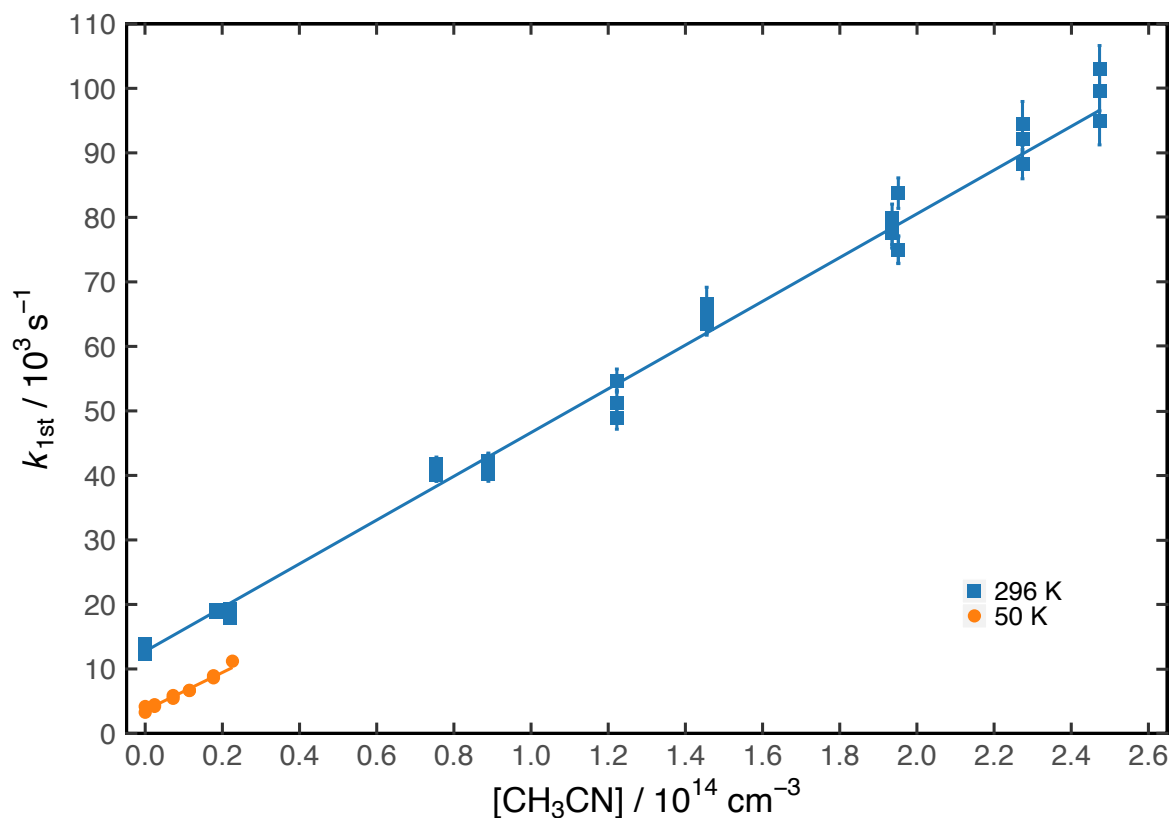


Figure 3 Variation of the pseudo-first-order rate constant, k_{1st} , as a function of the CH_3CN concentration. (Solid blue squares) measurements recorded at 296 K; (solid orange circles) measurements recorded at 50 K. Solid lines represent the weighted linear least-squares fits to the individual datasets. The uncertainties associated with each datapoint were derived from exponential fits such as those presented in Figure 1.

The y-axis intercept values shown in Figure 3 are the sum of the constant $\text{C}(^3\text{P})$ first-order loss terms described above. As a polar molecule with a large electric dipole moment of 3.92 D, CH_3CN was seen to form clusters readily at high gas-phase concentration levels. The onset of cluster formation was easily identifiable in the present measurements, by a plateau in the measured k_{1st} values with increasing CH_3CN . Consequently, only those k_{1st} values that varied linearly as a function of $[\text{CH}_3\text{CN}]$ were used to extract the second-order rate constants.

Although the range of CH₃CN concentrations that could be employed at room temperature allowed decay profiles with a large variation in the associated k_{1st} value to be recorded, the same cannot be said of the low temperature measurements. At both 75 K and 50 K, cluster formation was seen to occur at very low CH₃CN concentration levels ($> 3 \times 10^{13} \text{ cm}^{-3}$), making reliable measurements of the second-order rate constant at these temperatures more difficult. Table 1 summarizes the measured second-order rate constants and other relevant information such as the CH₃CN concentration ranges used at each temperature.

Table 1 Measured second-order rate constants for the C(³P) + CH₃CN reaction

T / K	N^b	[CH ₃ CN] / 10^{13} cm^{-3}	Flow density] / 10^{17} cm^{-3}	$k_{C(^3P)+CH_3CN}$ / $10^{-10} \text{ cm}^3 \text{ s}^{-1}$	Carrier gas
296	36	0 - 24.7	1.63	$(3.39 \pm 0.34)^c$	Ar
177 ± 2^a	33	0 - 9.0	0.94	(3.05 ± 0.32)	N ₂
127 ± 2	30	0 - 9.9	1.26	(3.60 ± 0.36)	Ar
75 ± 2	30	0 - 2.6	1.47	(3.77 ± 0.46)	Ar
50 ± 1	11	0 - 2.3	2.59	(2.93 ± 0.36)	Ar

^aUncertainties on the calculated temperatures represent the statistical (1σ) errors obtained from Pitot tube measurements of the impact pressure. ^bNumber of individual measurements.

^cUncertainties on the measured rate constants represent the combined statistical (1σ) and estimated systematic errors (10%).

The measured second-order rate constants are displayed as a function of temperature in Figure 4.

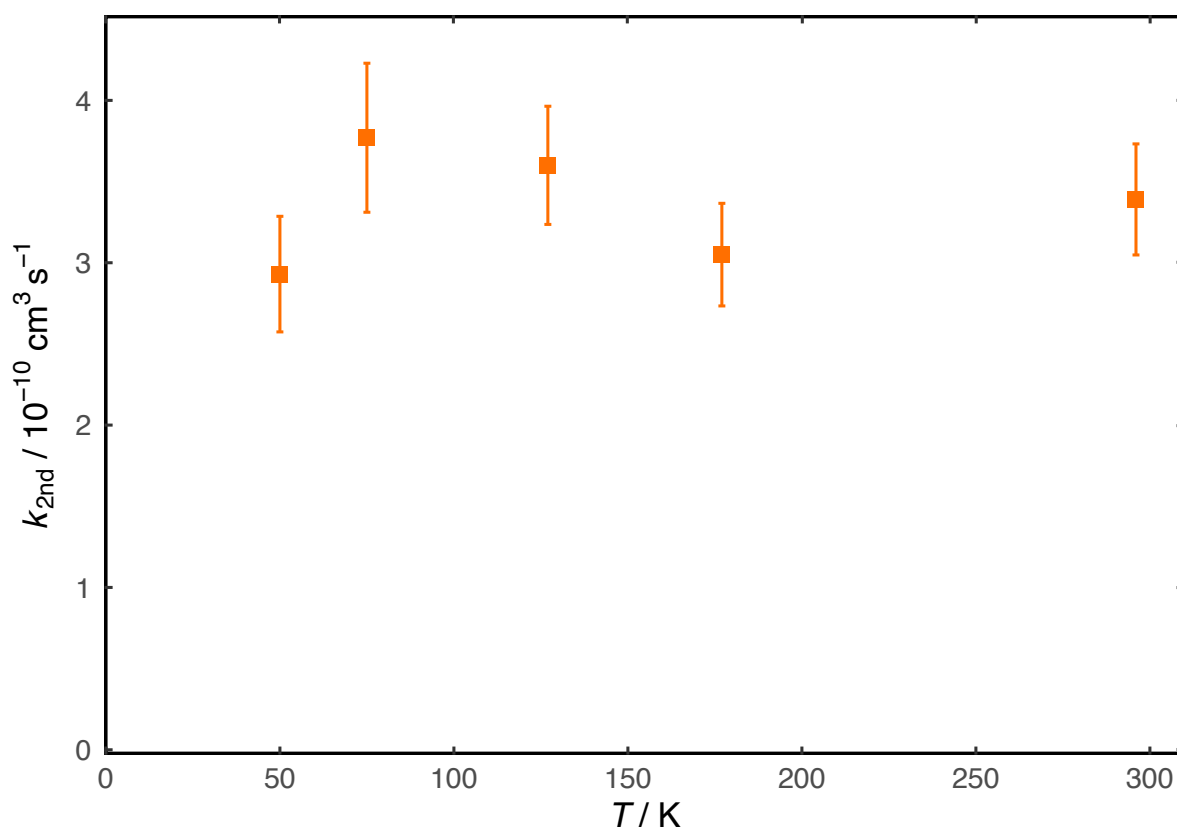


Figure 4 Measured rate constants for the $\text{C}(^3\text{P}) + \text{CH}_3\text{CN}$ reaction as a function of temperature. Uncertainties on the rate constants represent the combined statistical (1σ) and estimated systematic errors (10%).

The measured second-order rate constants are seen to be large ($3\text{-}4 \times 10^{-10} \text{ cm}^3 \text{ s}^{-1}$) reflecting the barrierless nature of the reaction. Considering the error bars, the reaction rate is also seen to be independent of temperature, with little or no variation over the entire temperature range. This is in contrast to other recent kinetic studies of other barrierless $\text{C}(^3\text{P})$ atom reactions with CH_3OH ²⁰ and NH_3 ²¹ as coreagents where the measured rate constants increased with decreasing temperature. Interestingly, these two processes are predicted to occur via the formation of a prereactive van der Waals type complex in the entrance channel followed by a reef-like transition state structure (below the reagent energy level) over the

PES connecting reagents with products. In contrast, the equivalent prereactive complex structure could not be located for the $C(^3P) + CH_3CN$ system at the MRCI+Q and DFT levels during this work. Previous theoretical studies of the $C(^3P) + C_2H_2$ reaction in particular⁴⁶ predict that this process also occurs without the presence of a saddle point in the entrance channel, while low temperature kinetic studies obtained rate constants that varied only slightly as a function of temperature.⁴⁷ Taken together, these studies suggest that the presence of a van de Waals complex is likely to be a prerequisite feature for the observation of a strong temperature dependence in $C(^3P)$ reactions.

4.2 Product Branching Ratios

To determine absolute H-atom product yields, H-atom VUV LIF signal intensities from the $C(^3P) + CH_3CN$ reaction were compared to those generated by the reaction between $C(^3P)$ and C_2H_4 . This process has a measured H-atom yield of 0.92 ± 0.04 at 300 K,⁴⁸ which we assume remains constant down to low temperature. Indeed, this reaction is not expected to display marked temperature and pressure dependences given the absence of an initial van der Waals complex and the presence of low submerged barriers leading from the C_3H_4 adduct to products $C_3H_3 + H$.⁴⁹ To ensure that the reactions of $C(^1D)$ atoms with CH_3CN and C_2H_4 did not interfere with the present experiments by producing additional H-atoms, N_2 was used as the carrier gas, generating a supersonic flow at 177 K. In addition, experiments were also conducted at 296 K (in the absence of a Laval nozzle) with N_2 as the carrier gas. The $C(^1D) + N_2 \rightarrow C(^3P) + N_2$ quenching reaction becomes more efficient as the temperature falls²⁴ with measured rate constants of $(5.3 \pm 0.5) \times 10^{-12} \text{ cm}^3 \text{ s}^{-1}$ at 296 K and a value around $7.5 \times 10^{-12} \text{ cm}^3 \text{ s}^{-1}$ at 177 K. Consequently, the $C(^1D)$ atoms generated by the photolysis of CBr_4 at 266 nm are expected to be removed under our experimental conditions within the first few

microseconds at both temperatures. Typical H-atom formation curves recorded sequentially for the C + CH₃CN and C + C₂H₄ reactions are shown in Figure 5.

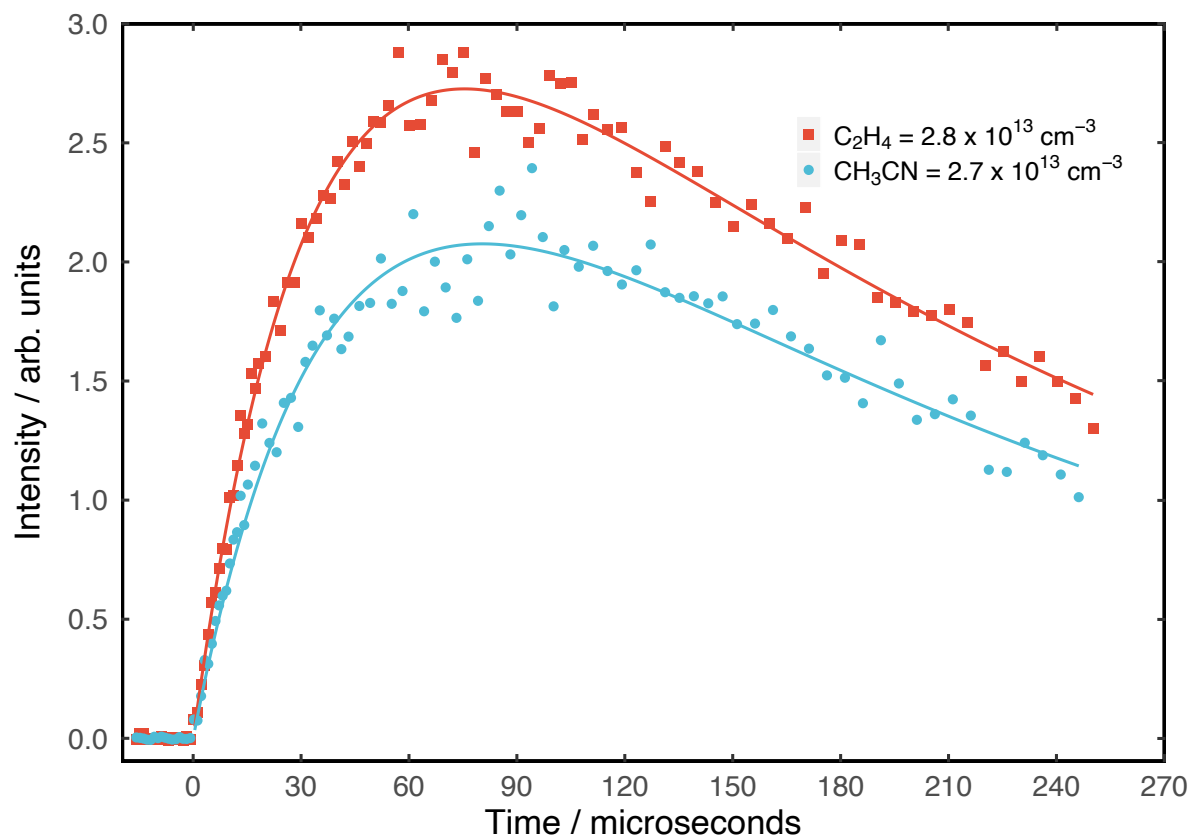


Figure 5 H-atom VUV LIF intensity as a function of delay time for the C + CH₃CN and C + C₂H₄ reactions recorded at 177 K. (Light blue solid circles) The C + CH₃CN reaction with [CH₃CN] = 2.7 × 10¹³ cm⁻³. (Red solid squares) The C + C₂H₄ reaction with [C₂H₄] = 2.8 × 10¹³ cm⁻³. Solid lines represent non-linear fits to the individual datasets using expression (2).

Several pairs of decays were recorded at each temperature, to minimize potential experimental errors. Moreover, the order in which the traces were acquired was alternated to reduce errors arising from possible variations of the fluorescence intensities with time. The H-atom fluorescence curves are well described by the following biexponential function

$$I_H = A\{\exp(-k_{L(H)}t) - \exp(-k_{1st}t)\} \quad (2)$$

where (I_H) is H-atom signal intensity and $k_{L(H)}$ represents secondary H-atom loss through processes such as diffusion. The first-order formation rate of atomic hydrogen, k_{1st} , is equal to $k_{C+X}[X] + k_{L(C)}$ where k_{C+X} is the rate constant for the reaction of C with X, with X representing either CH₃CN or C₂H₄. $k_{L(C)}$ represents secondary C-atom losses, such as through diffusion and secondary reactions. Consequently, it is important to use similar first-order-production rates when comparing H-atom intensities as can be seen in Figure 5, otherwise some carbon atoms could be lost without reacting with either of the coreagents. A represents the theoretical amplitude of the H-atom VUV LIF signal without secondary H-atom losses. In previous work, we used the derived A values for each reaction to obtain absolute H-atom yields. Nevertheless, the precision of the A factor values is highly dependent on the reproducibility of k_{1st} and $k_{L(H)}$ between traces; values which should remain constant throughout these experiments. As small variations in the derived k_{1st} and $k_{L(H)}$ fitting parameters led to significant variations in A in the present analysis, we chose instead to compare the peak values given by the biexponential fits to the data. The peak intensities of the H-atom formation curves for the C + C₂H₄ reference reaction were first divided by 0.92 to correct for the fact that the measured H-atom yields for this process are smaller than 1.⁴⁸ Absolute H-atom yields for the C(³P) + CH₃CN reaction were then obtained by dividing the peak values for the C(³P) + CH₃CN reaction by the corrected peak values for the C(³P) + C₂H₄ reaction. No corrections were required for VUV absorption losses in the present experiments as the low CH₃CN and C₂H₄ concentrations used here were estimated to result in less than 1 % absorption losses at 121.567 nm. The derived absolute H-atom yields for the C(³P) + CH₃CN reaction are listed in Table 2.

Table 2 Temperature dependent H-atom yields for the C(³P) + CH₃CN reaction

T / K	Number of experiments	Individual H-atom yields	Mean H-atom yield
296	7	0.63, 0.68, 0.63, 0.68, 0.63, 0.64, 0.59	0.64 ± 0.03 ^a
177	6	0.70, 0.68, 0.70, 0.58, 0.57, 0.56	0.63 ± 0.07

^aThe error bars reflect the statistical uncertainties at the 95 % confidence level.

The measured absolute H-atom yields for the C + CH₃CN reaction are significantly smaller than 1, indicating that other product channels not involving H-atom formation are important for this reaction. Moreover as the H-atom yields are constant between 177 K and 296 K, it is likely that the product branching ratios themselves do not change significantly as a function of temperature at least over the range of experimental temperatures. According to Figure 1, the most favourable products are likely to be H + CH₂CNC and H + CH₂CCN on the triplet surface as the channels leading to CH₃ + CNC and H + H + HC₃N are endothermic. Additionally, the channels C₂H₂ + HCN, C₂H₂ + HNC, H₂ + HC₃N and H₂ + HCCNC are all endothermic when one of these species is formed in its first triplet state. Consequently, if reaction occurs exclusively over the triplet surface, we would expect a H-atom yield close to 1 which is clearly not the case. As discussed in section 3, the close proximity and similar equilibrium geometries of triplet and singlet CH₃CNC might promote non-adiabatic coupling between the triplet and singlet surfaces, leading instead to the production of C₂H₃NC or C₂H₃CN in their ground singlet states, intermediates that are much more stable than those formed over the triplet surface as can be seen from Figure 1. These singlet species might then preferentially lead to the

formation of $C_2H_2 + HCN$, $C_2H_2 + HNC$ and $H_2 + HC_3N$ as products,⁴³ thereby explaining the measured H-atom yields significantly lower than unity.

5 Astrochemical Model

Given the absence of the $C + CH_3CN$ reaction from current astrochemical databases,⁵⁰ it is interesting to test the effect of this process on the abundances of CH_3CN and other related species predicted by astrochemical models. Here, we used the gas-grain model Nautilus^{51, 52} in its three-phase form⁵³ to simulate the abundances of atoms and molecules in neutral and ionic form as a function of time, employing kida.uva.2014⁵⁰ as the basic reaction network. 798 species are identified in the network that are involved in 8600 individual reactions. Elements are either initially in their atomic or ionic forms in this model (elements with an ionization potential < 13.6 eV are considered to be fully ionized) and the C/O elemental ratio is equal to 0.71 in this work. The initial simulation parameters are listed in Table 3.

Table 3 Elemental abundances and other model parameters

Element	Abundance ^(a)	$nH + 2nH_2 / cm^{-3}$	T/ K	Cosmic ray ionization rate / s^{-1}	Visual extinction
H ₂	0.5	2.5×10^4	10	1.3×10^{-17}	10
He	0.09				
C ⁺	1.7×10^{-4}				
N	6.2×10^{-5}				
O	2.4×10^{-4}				
S ⁺	1.5×10^{-5}				
Fe ⁺	3.0×10^{-9}				
Cl ⁺	1.0×10^{-9}				
F	6.7×10^{-9}				

^(a)Relative to total hydrogen ($nH + 2nH_2$)

The grain surface and the mantle are both chemically active for these simulations, while accretion and desorption are only allowed between the surface and the gas-phase. The dust-

to-gas ratio (in terms of mass) is 0.01. A sticking probability of 1 is assumed for all neutral species while desorption can occur by thermal and non-thermal (cosmic rays, chemical desorption) processes. Surface reactions proceed through the Langmuir-Hinshelwood mechanism (between reagents that are already adsorbed) while reagents must either overcome a diffusion barrier or tunnel through the barrier (particularly for light species such as H) to encounter the coreagent in a neighbouring site. For exothermic barrierless reactions the reaction probability is considered to be 1 once the two reagents occupy the same site. For activated exothermic reactions, the competition between reaction, diffusion out of the site and desorption to the gas-phase is considered to obtain the reaction probability. A more detailed description of the simulations can be found in Ruaud et al.⁵³

In dense molecular clouds, CH₃CN is mainly produced in the gas-phase through the HCN + CH₃⁺ → CH₃CNH⁺ + hv radiative association reaction⁵⁴⁻⁵⁶ followed by dissociative recombination, CH₃CNH⁺ + e⁻ → CH₃CN + H. In current networks the main destruction pathways are the reactions with H⁺, He⁺ and H₃⁺ as well as depletion onto grains.

As can be seen from Figure 6, introduction of the C + CH₃CN reaction with an estimated rate constant, $k_{C+CH_3CN}(10\text{ K}) = 3.4 \times 10^{-10} \text{ cm}^3 \text{ s}^{-1}$, leads to a maximum reduction of the CH₃CN abundance of more than two orders of magnitude between 10³ and 10⁵ years.

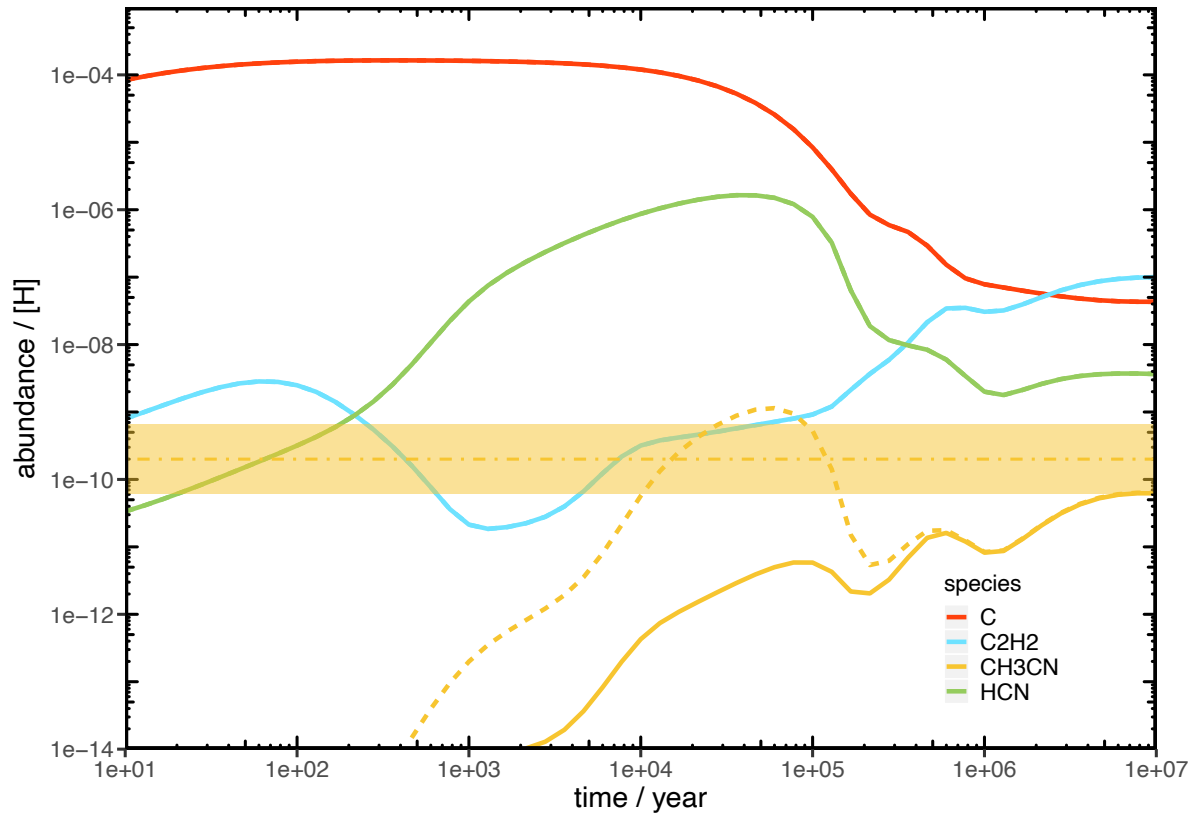


Figure 6 Gas-grain astrochemical model results for the formation of selected species in dark clouds as a function of cloud age. (Dashed lines) standard network results. (Solid lines) the same network but with the gas-phase C + CH₃CN reaction included. (Red lines) C(³P); (yellow lines) CH₃CN; (green lines) HCN; (blue lines) C₂H₂. (Yellow dashed dotted line) observed CH₃CN abundance in TMC-1.¹³ The yellow box represents arbitrary upper (nominal CH₃CN abundance × 3.3) and lower (nominal CH₃CN abundance / 3.3) limiting values for the CH₃CN abundance.

At ages considered to be characteristic of typical dense clouds ($> 2 \times 10^5$ years), atomic carbon is removed from the gas-phase by accretion onto grains, and/or through gas-phase reactions forming CO, thereby limiting the effect of the C + CH₃CN reaction. Although the standard model provided simulated CH₃CN abundances similar to the observational values, inclusion of the C + CH₃CN reaction in the network leads to predicted CH₃CN abundances that are

significantly underestimated (with a peak value at 1×10^5 years around 6×10^{-12} relative to total hydrogen ($n\text{H} + 2n\text{H}_2$)) compared to the observed one (around 2×10^{-10} in TMC-1¹³). This underestimation may be due to an underestimation of the rate of the $\text{HCN} + \text{CH}_3^+ \rightarrow \text{CH}_3\text{CNH}^+ + h\nu$ radiative association reaction but it could also result from an underestimation of the efficiency of H_2 ionization by cosmic rays, which is the origin of ion chemistry in dense interstellar clouds and whose value is only poorly constrained. Recent simulations also significantly underestimate gas-phase CH_3CN in other objects such as in the protostar IRAS 16293–2422.⁵⁷

Despite the effect of the $\text{C} + \text{CH}_3\text{CN}$ reaction on CH_3CN abundances at early times, these simulations indicate that the $\text{C} + \text{CH}_3\text{CN}$ reaction induces only small changes in the gas-phase abundance of CH_3CN at typical dense interstellar cloud ages (around a few 10^5 years). Similarly, this process also has only a weak effect on the abundance of CH_3CN on grains. Indeed, CH_3CN on grains is mainly generated by the hydrogenation of CH_2CN , itself produced in the gas-phase by the dissociative recombination of CH_3CNH^+ and by the $\text{CN} + \text{CH}_3 \rightarrow \text{H}_2\text{CCN} + \text{H}$ reaction followed by accretion of the CH_2CN radical onto interstellar grains.

Given the large discrepancy between the simulated and observed abundances of CH_3CN , it is clear that the chemistry of CH_3CN in the interstellar medium is quite poorly constrained and should be studied in more detail in the future. This is also true of the fate of the products of the $\text{C} + \text{CH}_3\text{CN}$ reaction. In the current network we have not introduced the products CH_2CCN and CH_2CNC (these species are not currently present in the KIDA database), replacing them instead by the probable products over the singlet surface, $\text{C}_2\text{H}_2 + \text{HCN}$. This simplification does not lead to large differences for either C_2H_2 or HCN (the abundance curves obtained with and without the $\text{C} + \text{CH}_3\text{CN}$ reaction are superimposed in Figure 6). Given the low abundance of CH_3CN , this does not significantly disrupt other parts of the network either, as the abundances

of products CH_2CCN and CH_2CNC will be relatively low. Moreover, the radical nature of these species make them likely to be reactive, in particular with abundant O, C, N and H atoms. However, even if the abundances of CH_2CCN and CH_2CNC are expected to be low, these species merit further study in the future as potential sources of complex molecules.

Apart from the direct impact of the $\text{C} + \text{CH}_3\text{CN}$ reaction on the abundance of CH_3CN in the interstellar medium, our study showing the absence of barrier for this reaction reinforces our understanding of the reactivity of atomic carbon with nitriles, with particular relevance to earlier work on the $\text{C} + \text{HNC}$ reaction,¹⁷ the $\text{C} + \text{HC}_3\text{N}$ reaction⁵⁸ and even the $^{13}\text{C} + \text{HCN} \rightarrow \text{C} + \text{H}^{13}\text{CN}$ carbon exchange reaction.⁵⁹

6 Conclusions

This work reports the result of a joint experimental and theoretical investigation of the $\text{C}(^3\text{P}) + \text{CH}_3\text{CN}$ reaction. On the experimental side, rate constants for this process were measured over the 50-296 K temperature range using a supersonic flow reactor. $\text{C}(^3\text{P})$ atoms were generated by the 266 nm pulsed laser photolysis of CBr_4 during this work which were detected directly by pulsed laser induced fluorescence at 115.8 nm. The reaction is seen to occur rapidly down to 50 K, displaying little or no temperature dependence. In addition, measurements of the kinetics of H-atom formation were also performed allowing quantitative H-atom product yields to be determined by comparison with the measured H-atom yields of the $\text{C} + \text{C}_2\text{H}_4$ reference reaction. On the theoretical side, electronic structure calculations were performed on the only attractive triplet surface ($^3\text{A}''$) of the three correlating with reagents using a multiconfigurational method. These calculations allowed us to derive the various intermediates, stationary points and possible product channels of the title reaction. In conjunction with the measurements, these results indicate that a significant

fraction of the overall reaction is likely to occur through a non-adiabatic process, possibly through intersystem crossing to the singlet surface leading instead to stable molecular products.

The new rate constants were introduced into a gas-grain model of dense interstellar clouds. These simulations showed that the predicted CH₃CN abundances decrease by more than two orders of magnitude at intermediate times, while the effect was seen to be considerably less important at typical cloud ages. As the predicted CH₃CN abundances significantly underestimate the observed values, further work is required to better understand the formation and destruction mechanisms of interstellar CH₃CN.

Author Information

Corresponding Author

*Email: kevin.hickson@u-bordeaux.fr.

Acknowledgements

K. M. H. acknowledges support from the French program “Physique et Chimie du Milieu Interstellaire” (PCMI) of the CNRS/INSU with the INC/INP co-funded by the CEA and CNES as well as funding from the “Programme National de Planétologie” (PNP) of the CNRS/INSU.

References

1. Hynes, A. J.; Wine, P. H., Kinetics and Mechanism of the Reaction of Hydroxyl Radicals with Acetonitrile under Atmospheric Conditions. *J. Phys. Chem.* **1991**, *95* (3), 1232-1240.
2. Tyndall, G. S.; Orlando, J. J.; Wallington, T. J.; Sehested, J.; Nielsen, O. J., Kinetics of the Reactions of Acetonitrile with Chlorine and Fluorine Atoms. *J. Phys. Chem.* **1996**, *100* (2), 660-668.
3. Hamm, S.; Warneck, P., The Interhemispheric Distribution and the Budget of Acetonitrile in the Troposphere. *J. Geophys. Res.: Atmos.* **1990**, *95* (D12), 20593-20606.
4. Harrison, J. J.; Bernath, P. F., ACE-FTS Observations of Acetonitrile in the Lower Stratosphere. *Atmos. Chem. Phys.* **2013**, *13* (15), 7405-7413.
5. Solomon, P. M.; Jefferts, K. B.; Penzias, A. A.; Wilson, R. W., Detection of Millimeter Emission Lines from Interstellar Methyl Cyanide. *Astrophys. J.* **1971**, *168*, L107.

6. Matthews, H. E.; Sears, T. J., Detection of the $J = 1 \rightarrow 0$ Transition of CH_3CN . *Astrophys. J.* **1983**, *267*, L53-L57.
7. Öberg, K. I.; Guzmán, V. V.; Furuya, K.; Qi, C.; Aikawa, Y.; Andrews, S. M.; Loomis, R.; Wilner, D. J., The Comet-Like Composition of a Protoplanetary Disk as Revealed by Complex Cyanides. *Nature* **2015**, *520*, 198-201.
8. Ulich, B. L.; Conklin, E. K., Detection of Methyl Cyanide in Comet Kohoutek. *Nature* **1974**, *248* (5444), 121-122.
9. Marten, A.; Hidayat, T.; Biraud, Y.; Moreno, R., New Millimeter Heterodyne Observations of Titan: Vertical Distributions of Nitriles HCN, HC_3N , CH_3CN , and the Isotopic Ratio $^{15}\text{N}/^{14}\text{N}$ in Its Atmosphere. *Icarus* **2002**, *158* (2), 532-544.
10. Gerin, M.; Combes, F.; Wlodarczak, G.; Jacq, T.; Guelin, M.; Encrenaz, P.; Laurent, C., Interstellar Detection of Deuterated Methyl Cyanide. *Astron. Astrophys.* **1992**, *259*, L35-L38.
11. Calcutt, H.; Jørgensen, J. K.; Müller, H. S. P.; Kristensen, L. E.; Coutens, A.; Bourke, T. L.; Garrod, R. T.; Persson, M. V.; van der Wiel, M. H. D.; van Dishoeck, E. F.; Wampfler, S. F., The ALMA-PILS Survey: Complex Nitriles Towards IRAS 16293–2422. *Astron. Astrophys.* **2018**, *616*.
12. Iino, T.; Sagawa, H.; Tsukagoshi, T., $^{14}\text{N}/^{15}\text{N}$ Isotopic Ratio in CH_3CN of Titan's Atmosphere Measured with ALMA. *Astrophys. J.* **2020**, *890* (2), 95.
13. Gratier, P.; Majumdar, L.; Ohishi, M.; Roueff, E.; Loison, J. C.; Hickson, K. M.; Wakelam, V., A New Reference Chemical Composition for TMC-1. *Astrophys. J., Suppl. Ser.* **2016**, *225* (2), 25.
14. Jamieson, J. W. S.; Brown, G. R.; Tanner, J. S., The Reaction of Atomic Hydrogen with Methyl Cyanide. *Can. J. Chem.* **1970**, *48* (23), 3619-3622.
15. Budge, S.; Roscoe, J. M., The Reactions of $\text{O}(^3\text{P})$ with Acetonitrile and Propionitrile. *Can. J. Chem.* **1995**, *73* (5), 666-674.
16. Dutuit, O.; Carrasco, N.; Thissen, R.; Vuitton, V.; Alcaraz, C.; Pernot, P.; Balucani, N.; Casavecchia, P.; Canosa, A.; Le Picard, S.; Loison, J. C.; Herman, Z.; Zabka, J.; Ascenzi, D.; Tosi, P.; Franceschi, P.; Price, S. D.; Lavvas, P., Critical Review of N , N^+ , N_2^+ , N^{++} , and N_2^{++} Main Production Processes and Reactions of Relevance to Titan's Atmosphere. *Astrophys. J., Suppl. Ser.* **2013**, *204* (2), 20-66.
17. Loison, J. C.; Hickson, K. M., Ab Initio Study of the $\text{C}+\text{HNC}$, $\text{N}+\text{C}_2\text{H}$, $\text{H}+\text{C}_2\text{N}$ and $\text{H}+\text{CNC}$ Reactions. *Chem. Phys. Lett.* **2015**, *635*, 174-179.
18. Daugey, N.; Caubet, P.; Bergeat, A.; Costes, M.; Hickson, K. M., Reaction Kinetics to Low Temperatures. Dicarbon + Acetylene, Methylacetylene, Allene and Propene from $77 \leq T \leq 296$ K. *Phys. Chem. Chem. Phys.* **2008**, *10* (5), 729-737.
19. Daugey, N.; Caubet, P.; Retail, B.; Costes, M.; Bergeat, A.; Dorthe, G., Kinetic Measurements on Methylidyne Radical Reactions with Several Hydrocarbons at Low Temperatures. *Phys. Chem. Chem. Phys.* **2005**, *7* (15), 2921-7.
20. Shannon, R. J.; Cossou, C.; Loison, J.-C.; Caubet, P.; Balucani, N.; Seakins, P. W.; Wakelam, V.; Hickson, K. M., The Fast $\text{C}(^3\text{P}) + \text{CH}_3\text{OH}$ Reaction as an Efficient Loss Process for Gas-Phase Interstellar Methanol. *RSC Adv.* **2014**, *4* (50), 26342.
21. Hickson, K. M.; Loison, J.-C.; Bourgalais, J.; Capron, M.; Le Picard, S. D.; Goulay, F.; Wakelam, V., The $\text{C}(^3\text{P}) + \text{NH}_3$ Reaction in Interstellar Chemistry. II. Low Temperature Rate Constants and Modeling of NH , NH_2 , and NH_3 Abundances in Dense Interstellar Clouds. *Astrophys. J.* **2015**, *812* (2), 107.

22. Hickson, K. M.; Loison, J.-C.; Nuñez-Reyes, D.; Méreau, R., Quantum Tunneling Enhancement of the C + H₂O and C + D₂O Reactions at Low Temperature. *J. Phys. Chem. Lett.* **2016**, *7* (18), 3641-3646.
23. Hickson, K. M.; Loison, J.-C.; Guo, H.; Suleimanov, Y. V., Ring-Polymer Molecular Dynamics for the Prediction of Low-Temperature Rates: An Investigation of the C(¹D) + H₂ Reaction. *J. Phys. Chem. Lett.* **2015**, *6*, 4194-4199.
24. Hickson, K. M.; Loison, J.-C.; Lique, F.; Kłos, J., An Experimental and Theoretical Investigation of the C(¹D) + N₂ → C(³P) + N₂ Quenching Reaction at Low Temperature. *J. Phys. Chem. A* **2016**, *120* (16), 2504-2513.
25. Hickson, K. M.; Suleimanov, Y. V., An Experimental and Theoretical Investigation of the C(¹D) + D₂ Reaction. *Phys. Chem. Chem. Phys.* **2017**, *19* (1), 480-486.
26. Nuñez-Reyes, D.; Hickson, K. M., Kinetic and Product Study of the Reactions of C(¹D) with CH₄ and C₂H₆ at Low Temperature. *J. Phys. Chem. A* **2017**, *121* (20), 3851-3857.
27. Nuñez-Reyes, D.; Hickson, K. M., The Reactivity of C(¹D) with Oxygen Bearing Molecules NO and O₂ at Low Temperature. *Chem. Phys. Lett.* **2017**, *687*, 330-335.
28. Nuñez-Reyes, D.; Hickson, K. M., Kinetics of the Gas-Phase O(¹D) + CO₂ and C(¹D) + CO₂ Reactions over the 50–296 K Range. *J. Phys. Chem. A* **2018**, *122* (16), 4002-4008.
29. Wu, Y.; Cao, J.; Ma, H.; Zhang, C.; Bian, W.; Nunez-Reyes, D.; Hickson, K. M., Conical Intersection-Regulated Intermediates in Bimolecular Reactions: Insights from the Product Branching Ratio of the C(¹D) + HD Reaction. *Sci. Adv.* **2019**, *5* (4), eaaw0446.
30. Hickson, K. M., Low-Temperature Rate Constants and Product-Branching Ratios for the C(¹D) + H₂O Reaction. *J. Phys. Chem. A* **2019**, *123* (25), 5206-5213.
31. Nuñez-Reyes, D.; Hickson, K. M., A Low Temperature Investigation of the Gas-Phase N(²D) + NO Reaction. Towards a Viable Source of N(²D) Atoms for Kinetic Studies in Astrochemistry. *Phys. Chem. Chem. Phys.* **2018**, *20* (25), 17442-17447.
32. Nuñez-Reyes, D.; Loison, J.-C.; Hickson, K. M.; Dobrijevic, M., A Low Temperature Investigation of the N(²D) + CH₄, C₂H₆ and C₃H₈ Reactions. *Phys. Chem. Chem. Phys.* **2019**, *21* (12), 6574-6581.
33. Nuñez-Reyes, D.; Loison, J.-C.; Hickson, K. M.; Dobrijevic, M., Rate Constants for the N(²D) + C₂H₂ Reaction over the 50–296 K Temperature Range. *Phys. Chem. Chem. Phys.* **2019**, *21* (40), 22230-22237.
34. Grondin, R.; Loison, J.-C.; Hickson, K. M., Low Temperature Rate Constants for the Reactions of O(¹D) with N₂, O₂, and Ar. *J. Phys. Chem. A* **2016**, *120* (27), 4838-4844.
35. Hickson, K. M.; Suleimanov, Y. V., Low-Temperature Experimental and Theoretical Rate Constants for the O(¹D) + H₂ Reaction. *J. Phys. Chem. A* **2017**, *121* (9), 1916-1923.
36. Meng, Q. Y.; Hickson, K. M.; Shao, K. J.; Loison, J. C.; Zhang, D. H., Theoretical and Experimental Investigations of Rate Coefficients of O(¹D) + CH₄ at Low Temperature. *Phys. Chem. Chem. Phys.* **2016**, *18* (42), 29286-29292.
37. Nuñez-Reyes, D.; Hickson, K. M.; Larrégaray, P.; Bonnet, L.; González-Lezana, T.; Suleimanov, Y. V., A Combined Theoretical and Experimental Investigation of the Kinetics and Dynamics of the O(¹D) + D₂ Reaction at Low Temperature. *Phys. Chem. Chem. Phys.* **2018**, *20* (6), 4404-4414.
38. Nuñez-Reyes, D.; Kłos, J.; Alexander, M. H.; Dagdigian, P. J.; Hickson, K. M., Experimental and Theoretical Investigation of the Temperature Dependent Electronic Quenching of O(¹D) Atoms in Collisions with Kr. *J. Chem. Phys.* **2018**, *148* (12), 124311.

39. Nuñez-Reyes, D.; Hickson, K. M.; Larrégaray, P.; Bonnet, L.; González-Lezana, T.; Bhowmick, S.; Suleimanov, Y. V., Experimental and Theoretical Study of the O(¹D) + HD Reaction. *J. Phys. Chem. A* **2019**, *123* (38), 8089-8098.
40. Ewing, M. B.; Ochoa, J. C. S., Vapor Pressures of Acetonitrile Determined by Comparative Ebulliometry. *J. Chem. Eng. Data* **2004**, *49* (3), 486-491.
41. Bourgalais, J.; Capron, M.; Kailasanathan, R. K. A.; Osborn, D. L.; Hickson, K. M.; Loison, J.-C.; Wakelam, V.; Goulay, F.; Le Picard, S. D., The C(³P) + NH₃ Reaction in Interstellar Chemistry. I. Investigation of the Product Formation Channels. *Astrophys. J.* **2015**, *812* (2), 106.
42. Zhao, Y.; Truhlar, D., The M06 Suite of Density Functionals for Main Group Thermochemistry, Thermochemical Kinetics, Noncovalent Interactions, Excited States, and Transition Elements: Two New Functionals and Systematic Testing of Four M06-Class Functionals and 12 Other Functionals. *Theor. Chem. Acc.* **2008**, *120* (1), 215-241.
43. Homayoon, Z.; Vásquez, S. A.; Rodríguez-Fernández, R.; Martínez-Nuñez, E., Ab Initio and RRKM Study of the HCN/HNC Elimination Channels from Vinyl Cyanide. *J. Phys. Chem. A* **2011**, *115* (6), 979-985.
44. Zaleski, D. P.; Harding, L. B.; Klippenstein, S. J.; Ruscic, B.; Prozument, K., Time-Resolved Kinetic Chirped-Pulse Rotational Spectroscopy in a Room-Temperature Flow Reactor. *J. Phys. Chem. Lett.* **2017**, *8* (24), 6180-6188.
45. Prozument, K.; Baraban, J. H.; Bryan Changala, P.; Barratt Park, G.; Shaver, R. G.; Muentner, J. S.; Klippenstein, S. J.; Chernyak, V. Y.; Field, R. W., Photodissociation Transition States Characterized by Chirped Pulse Millimeter Wave Spectroscopy. *Proc. Natl. Acad. Sci. U. S. A.*, **2020**, *117* (1), 146-151.
46. Ochsenfeld, C.; Kaiser, R. I.; Lee, Y. T.; Suits, A. G.; Head-Gordon, M., A Coupled-Cluster Ab Initio Study of Triplet C₃H₂ and the Neutral-Neutral Reaction to Interstellar C₃H. *J. Chem. Phys.* **1997**, *106* (10), 4141-4151.
47. Chastaing, D.; Le Picard, S. D.; Sims, I. R.; Smith, I. W. M., Rate Coefficients for the Reactions of C(³P_j) Atoms with C₂H₂, C₂H₄, CH₃C≡CH and H₂C=C=CH₂ at Temperatures Down to 15 K. *Astron. Astrophys.* **2001**, *365* (2), 241-247.
48. Bergeat, A.; Loison, J.-C., Reaction of Carbon Atoms, C(²P₂, ³P) with and C₂H₂, C₂H₄ and C₆H₆: Overall Rate Constant and Relative Atomic Hydrogen Production. *Phys. Chem. Chem. Phys.* **2001**, *3*, 2038.
49. Le, T. N.; Lee, H.-Y.; Mebel, A. M.; Kaiser, R. I. Ab Initio MO Study of the Triplet C₃H₄ Potential Energy Surface and the Reaction of C(³P_j) with Ethylene, C₂H₄. *J. Phys. Chem. A* **2001**, *105*, 1847-1856.
50. Wakelam, V.; Loison, J. C.; Herbst, E.; Pavone, B.; Bergeat, A.; Béroff, K.; Chabot, M.; Faure, A.; Galli, D.; Geppert, W. D.; Gerlich, D.; Gratier, P.; Harada, N.; Hickson, K. M.; Honvault, P.; Klippenstein, S. J.; Le Picard, S. D.; Nyman, G.; Ruaud, M.; Schlemmer, S.; Sims, I. R.; Talbi, D.; Tennyson, J.; Wester, R., The 2014 KIDA Network for Interstellar Chemistry. *Astrophys. J., Suppl. Ser.* **2015**, *217* (2), 20.
51. Hersant, F.; Wakelam, V.; Dutrey, A.; Guilloteau, S.; Herbst, E., Cold CO in Circumstellar Disks. *Astron. Astrophys.* **2009**, *493* (3), L49-L52.
52. Semenov, D.; Hersant, F.; Wakelam, V.; Dutrey, A.; Chapillon, E.; Guilloteau, S.; Henning, T.; Launhardt, R.; Piétu, V.; Schreyer, K., Chemistry in Disks. *Astron. Astrophys.* **2010**, *522*, A42.

53. Ruaud, M.; Wakelam, V.; Hersant, F., Gas and Grain Chemical Composition in Cold Cores as Predicted by the Nautilus Three-Phase Model. *Mon. Not. R. Astron. Soc.* **2016**, *459* (4), 3756-3767.
54. McEwan, M. J.; Anicich, V. G.; Huntress, W. T.; Kemper, P. R.; Bowers, M. T., A Low Pressure Study of the Reaction $\text{CH}_3^+ + \text{HCN} \rightarrow \text{CH}_3\cdot\text{HCN}^+$: A Case for Radiative Association. *Chem. Phys. Lett.* **1980**, *75* (2), 278-282.
55. Bass, L. M.; Kemper, P. R.; Anicich, V. G.; Bowers, M. T., Ion-Molecule Radiative Association Reactions. A Statistical Phase Space Theory Model. *J. Am. Chem. Soc.* **1981**, *103*, 5283-5292.
56. Klippenstein, S. J.; Yang, Y.-C.; Ryzhov, V.; Dunbar, R. C., Theory and Modeling of Ion--Molecule Radiative Association Kinetics. *J. Chem. Phys.* **1996**, *104* (12), 4502-4516.
57. Andron, I.; Gratier, P.; Majumdar, L.; Vidal, T. H. G.; Coutens, A.; Loison, J.-C.; Wakelam, V., Methyl Cyanide (CH_3CN) and Propyne (CH_3CCH) in the Low-Mass Protostar Iras 16293–2422. *Mon. Not. R. Astron. Soc.* **2018**, *481* (4), 5651-5659.
58. Li, H. Y.; Cheng, W. C.; Liu, Y. L.; Sun, B. J.; Huang, C. Y.; Chen, K. T.; Tang, M. S.; Kaiser, R. I.; Chang, A. H. H., Reaction of Cyanoacetylene $\text{HCCCN}(X^1\Sigma^+)$ with Ground-State Carbon Atoms $\text{C}(^3\text{P})$ in Cold Molecular Clouds. *J. Chem. Phys.* **2006**, *124* (4), 044307-19.
59. Loison, J.-C.; Wakelam, V.; Gratier, P.; Hickson, K. M., Gas-Grain Model of Carbon Fractionation in Dense Molecular Clouds. *Mon. Not. R. Astron. Soc.* **2020**, *498* (4), 4663-4679.